# Spheroidal harmonics for generalizing the morphological decomposition of closed parametric surfaces

Supplementary Information

## SI-1 Inverse coordinates and bijective mapping

### SI-1.1 On the star-shaped (SS) and non-star-shaped (NSS) particles and their bijectivity

Here we define SS particles as those particles for which a bijective map is obtained using the radial mapping technique. Since the difference between SH and rSOH is simply a rescaling of the aspect ratio, particles that are SS can be parametrized with a bijective map for either of these two techniques. There is, however, a subtle difference between these two radial approaches, and the hyperbolic mapping (hSOH) discussed in the main text. To illustrate this, Figure SI-1A shows a manually generated SS stone, and SI-1B shows a manually generated NSS stone. Each subfigure shows a hyperbolic mapping (left panel) as well as a radial mapping (right panel). The radial and hyperbolic mappings slide the surface sampled points onto the target spheroid along the corresponding coordinate lines, shown with blue-dashed lines in each panel. As shown in this example, in most cases a (N)SS stone (i.e. (non-)bijective under radial mapping) will give a (non-)bijective hyperbolic mapping as well. However, given the curvature of the hyperbolic coordinate lines, this is not always guaranteed and could even depend on the chosen domain parameter $e$. Therefore, we always check for each stone whether a bijective map exists for the applied mapping.

To do so, we assume that the input surface normals (green arrows) always point outward of the stone bulk (away from the gray shading). In this case, the spheroidal parameterization directors for SS surfaces will all point outward as well. If one or more of the normals flip direction, then the mapping of the triangulated surface is nonbijective or the surface is nonmanifold. This can also be expressed through the difference between the normal of the surface at a point, and the normal of the spheroid at the same point is larger than $\pi/2$, we have a nonbijective mapping. It should be noted that nonmanifold surfaces can cause normal flips, but in this paper, we assume that all the input meshes are manifold and the normals of the input surface are consistent (all point inwards or all point outwards).

This yields a simple numerical check for the bijectivity of discrete manifold surfaces. To numerically check that, we define a map $n : \mathcal{M} \to \mathbb{S}^2$, where $n$ is the Gaussian map and $n(p_i)$ is the normal vector at a given point $p_i$ that lies on $\mathcal{M}$. The sign of the computed normals can be found via the signed area of each face. The mapping is bijective when all the normals point outward.

### SI-1.2 Analytic inverse spheroidal coordinates

For completeness, this section shows the derivation of the exact oblate and prolate spheroidal inverse coordinates. This is important for computing the proposed hyperbolic mapping. Analogous to radial vectors in spherical coordinates, the normal directors of a spheroid are hyperbolic sections. For radial mappings, we can normalize the directors of each point on the input surface resulting in a spheroidal image of the surface denoted $\mathcal{E}$. In this paper, we use this analytic approach to normalize the directors and compute the parameterization of a surface onto a target spheroid.

On the complex plane, we assume that the oblate coordinates are connected by the relation $\rho_{ob} + iz$, where

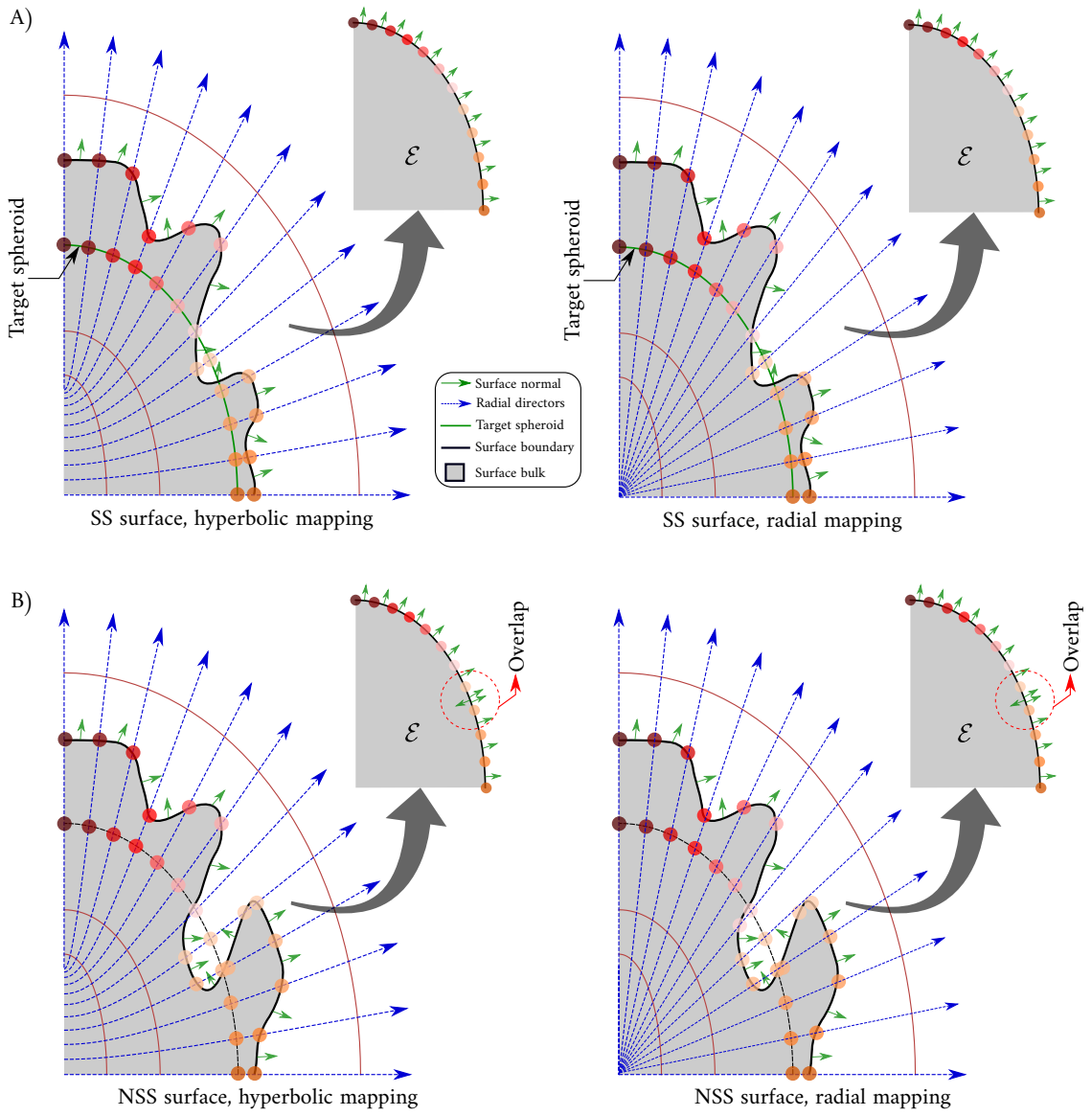


Figure SI-1: A cross-sectional view through a star-shaped stone (A) and non-star-shaped stone (B), subject to hyperbolic mapping (left) and radial mapping (right). The color-coded dots on the *target* spheroid are the result of sliding the sampled points from the discretized input surface along the coordinate lines onto the spheroidal space (blue-dashed lines; hyperbolic sections for hyperbolic mapping and straight lines for the radial mapping). In this example, both mappings are bijective in A, whereas both mappings are non-bijective in B.

$\rho_{ob} = \sqrt{x^2 + y^2}$. Now, we use the definition of the oblate spheroidal coordinates:

$$\begin{aligned} x(\zeta, \eta, \phi) &= e\ \cosh\zeta\ \cos\eta\ \cos\phi, \\ y(\zeta, \eta, \phi) &= e\ \cosh\zeta\ \cos\eta\ \sin\phi, \\ z(\zeta, \eta) &= e\ \sinh\zeta\ \sin\eta, \end{aligned} \tag{1}$$

We can rewrite $\rho_{ob}$ for the oblate coordinates as $\rho_{ob} = e\ \cosh\zeta\cos\eta$ and it follows from that:

$$\rho_{ob} + iz = e\ \left(\cosh\zeta\cos\eta + i\sinh\zeta\sin\eta\right). \tag{2}$$

We also know that the trigonometric and hyperbolic functions can be written in terms of Euler's formula such as:

$$\cos x = \frac{e^{ix} + e^{-ix}}{2}, \sin x = \frac{e^{ix} - e^{-ix}}{2i}, \tag{3}$$

$$\cosh x = \frac{e^{x} + e^{-x}}{2}, \sinh x = \frac{e^{x} - e^{-x}}{2}. \tag{4}$$

By comparison, we can also write $\sinh x = -i \sin(ix)$ and $\cos x = \cosh(ix)$. Substituting all these identities in Eq. (2) we obtain:

$$\rho_{ob} + iz = e \cosh(\zeta + i\eta). \tag{5}$$

The latter can be used for computing both $\zeta$ and $\eta$ coordinates such that:

$$\eta = \Im \left\{ \cosh^{-1} \left( \frac{\rho_{ob} + iz}{e} \right) \right\}, \quad \zeta = \Re \left\{ \cosh^{-1} \left( \frac{\rho_{ob} + iz}{e} \right) \right\}. \tag{6}$$

Similar to the above, we can derive the prolate coordinates. Though, for the prolate spheroids the complex plane is rotated by $\pi/2$. So, the complex plane relation for prolate coordinates becomes $i\rho_{pr}(\eta, \phi) + z$. Similarly, we obtain:

$$\eta = \Im \left\{ \cosh^{-1} \left( \frac{i\rho_{pr} + z}{e} \right) \right\}, \quad \zeta = \Re \left\{ \cosh^{-1} \left( \frac{i\rho_{pr} + z}{e} \right) \right\}. \tag{7}$$

These analytic formulae can be used to compute the hyperbolic mapping onto any spheroid when normalizing the hyperbolic normal directors by $\zeta = \zeta_0$. This approach is also used as a starting point for the discussion in SI-1.1.

### SI-1.3 Radial-based approximation of inverse spheroidal coordinates

In this section, we derive a radial-based approximation of the inverse spheroidal coordinates given the analytic ones explained in SI-1.2. This radial inversion is used for computing $\hat{\eta}$-coordinates that we used for the radial mapping to replace the $\eta$-coordinates (hyperbolic curves). To demonstrate this, we here consider a simple, but not less general, case in the elliptic coordinates in the plane $\phi = 0$, which can be written in the parametric form:

$$x(\zeta, \eta) = e \cosh \zeta \cos \eta,$$
$$z(\zeta, \eta) = e \sinh \zeta \sin \eta,$$

where $\zeta$ and $\eta$ are the exact spheroidal coordinates associated with Cartesian coordinates $x$ and $z$. In this radial mapping approach, we propose to normalize these coordinates such that:

$$\hat{x}(\zeta, \eta) = \frac{x(\zeta, \eta)}{e \cosh \zeta_0} = \frac{\cosh \zeta}{\cosh \zeta_0} \cos \eta, \tag{8}$$

$$\hat{z}(\zeta, \eta) = \frac{z(\zeta, \eta)}{e \sinh \zeta_0} = \frac{\sinh \zeta}{\sinh \zeta_0} \sin \eta, \tag{9}$$

where $\zeta_0$ defines a *target* elliptic section. From this, we can introduce the coordinate $\hat{\eta}$, such that:

$$\tan \hat{\eta} = \frac{\hat{z}(\zeta, \eta)}{\hat{x}(\zeta, \eta)} \tag{10}$$

$$= \frac{\sinh \zeta}{\cosh \zeta} \frac{\cosh \zeta_0}{\sinh \zeta_0} \frac{\sin \eta}{\cos \eta} \tag{11}$$

$$= \frac{\tanh \zeta}{\tanh \zeta_0} \tan \eta. \tag{12}$$

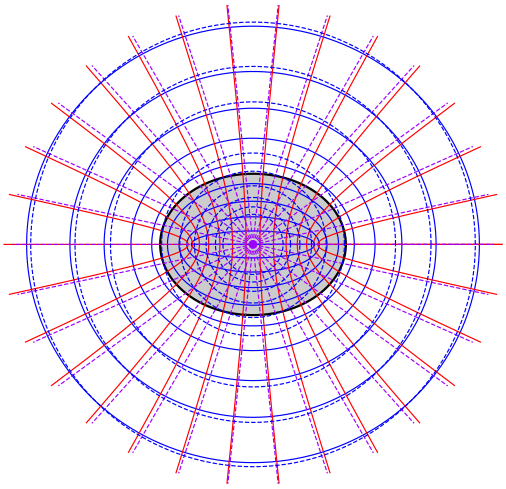

Figure SI-2: An overlay of the polar coordinates system on top of the elliptic one. The linear radials asymptotically approach the hyperbolic directors in the elliptic coordinate system. Solid lines represent the elliptic system with hyperbolic directors and confocal ellipses, while the dashed lines represent the radial directors with confocal circles.

Rewriting $\zeta = \zeta_0 + \epsilon$ and expanding in $\epsilon$, we obtain :

$$\tan\hat{\eta} = \frac{\tanh(\zeta_0+\epsilon)}{\tanh\zeta_0}\tan\eta = \tan\eta\left[1 + \frac{\epsilon}{\sinh\zeta_0\ \cosh\zeta_0} - \frac{\epsilon^2}{\cosh^2\zeta_0} + \mathcal{O}(\epsilon^3)\right]. \tag{13}$$

From Eq. (13), we can see that for points that fall on the $\zeta_0$-ellipse (or spheroid in 3D) $\hat{\eta} = \eta$. For points away from the target shape the difference between $\eta$ and $\hat{\eta}$ increases with $\zeta - \zeta_0$. Consequently, choosing $\hat{\eta}$ instead of $\eta$ can be seen as a linearization (first-order approximation) in the parametric difference $\zeta - \zeta_0$. Figure SI-2 shows how the linear radials converge to the hyperbolic directors of the elliptic coordinates. In general, we approach polar coordinates from the elliptic ones when $e \to 0$ while $\cosh\zeta \to \sinh\zeta$.

The approach is generalized for spheroids by replacing $x(\zeta,\eta)$ by $\rho(\zeta,\eta,\phi)$ that can be either normalized by $e\cosh\zeta_0$ or $e\sinh\zeta_0$ for oblate and prolate surfaces, respectively, in the spheroidal space.

### SI-1.4 Radial and hyperbolic mappings with the elliptic Fourier descriptors (EFD)–2D counterpart examples

To visualize the differences between the radial and hyperbolic mappings proposed here, we use the elliptic Fourier descriptor (EFD) approach (Kuhl and Giardina, 1982; Mollon and Zhao, 2012) to study the reconstruction of 2D closed contours. We further study the effect of these mappings on the orthogonality of the constructed basis functions as they directly affect the quality of the analysis and reconstruction. Here we have generated an SS contour that resembles a 2D cross-section of a stone and sampled it uniformly with a set of points (constant arc length between the points).

In Figure SI-3, we show the results of mapping the points using a hyperbolic map (A) and a radial map (B). The mapped points are again visualized using an arbitrary "target ellipse". Further, we use a similar least squares approach as in 3D to integrate the Fourier basis functions. This also allows us to further investigate the orthogonality of the discrete basis as a function of the sampling approaches. The results, on the same figure, show that the hyperbolic mapping favors sampling points near the poles (high-curvature areas), while the radial mapping favors sampling denser far from the poles (low-curvature areas). The effect of these mappings is shown in the middle column of sets (A) and (B) where we see oscillations occurring near the pole areas in the radial mapping due to the poor regularization in that area and weak sampling. Moreover,

the right column of the figure shows the corresponding orthogonality matrix for the constructed Fourier basis using $\eta$ for the hyperbolic mapping and $\hat{\eta}$ for the radial one where the error for the radial basis shows more off-orthogonality error.

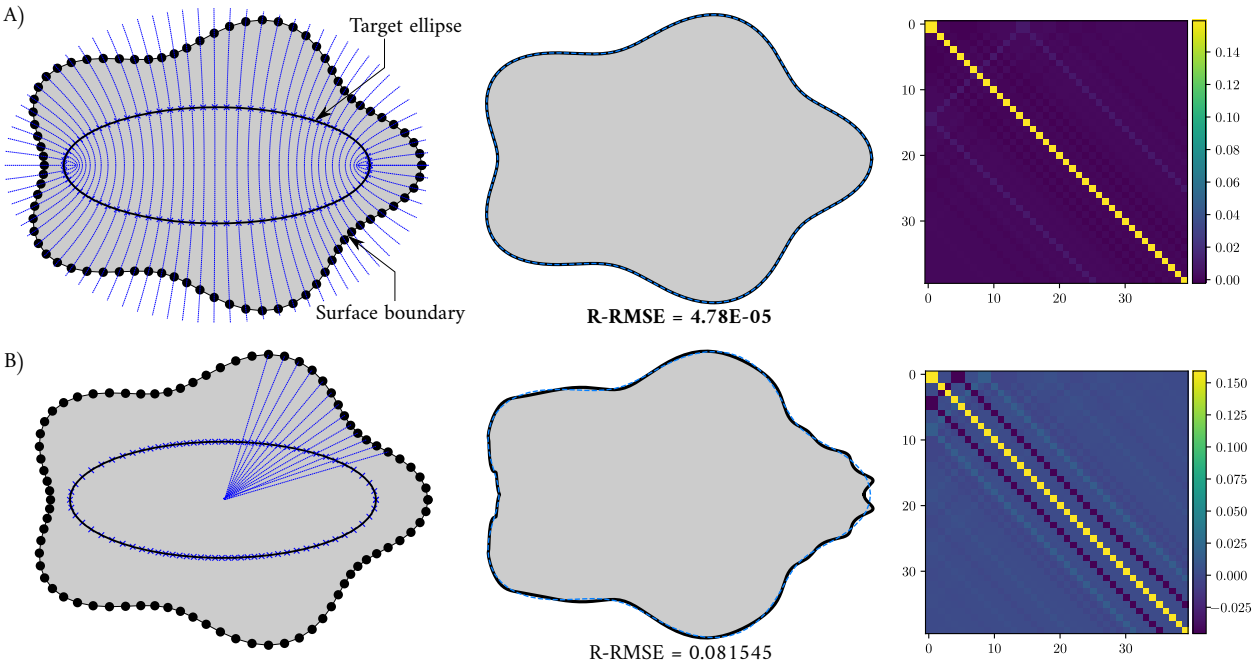


Figure SI-3: A comparison between the radial and hyperbolic mappings for 2D contours. (A) the left column shows the hyperbolic mapping onto an ellipse and the middle column is the corresponding reconstruction at $n_{max} = 20$ (the solid black line) as well as the right column is the orthogonality error matrix. (B) the left column same as the (A) but for the radial mapping. The blue-hashed lines in the middle column correspond to the original input surface contour. For this example, we used 141 points (for the herein renders we used only 51 points) to represent each contour and we sampled the $\eta$-coordinate with equal increments on each contour; the shown scatter on the left side does not represent the real count of the used points.

To further investigate the effect of the point distribution after mapping, we artificially distributed the *source* points in three different ways. In the first approach, we created source points so that the $\eta$ coordinate is uniformly sampled after mapping (see Fig. SI-4A). In the second approach, we created source points more densely near the pole area (see Fig. SI-4B). For the third one, we created most of the points near the low curvature areas (see Fig. SI-4C). After reconstructing the three cases, we find that the best results were obtained by the first approach. However, the results of the second approach were very close to the first one, while the third one deteriorated much faster for the same number of sampled points. This demonstrates that approaches that favor sampling more uniformly or even denser near the poles are in general better than those oversampling the low-curvature regions. This supports the main results in the manuscript that hyperbolic-based mapping is more beneficial than radial-based mapping.

Finally, to consider a more realistic example, we used random sampling on the input surface itself. By fixing the random seed number, we tested both the hyperbolic and radial sampling approaches onto the same target spheroid. Figure SI-5 shows the numerical differences between the hyperbolic and radial mapping and the arc-length distortion for the resulting target spheroid. The hyperbolic sampling was generally more preserving in terms of the arc length (equivalent to area-preserving in the 3D case) and orthogonality.

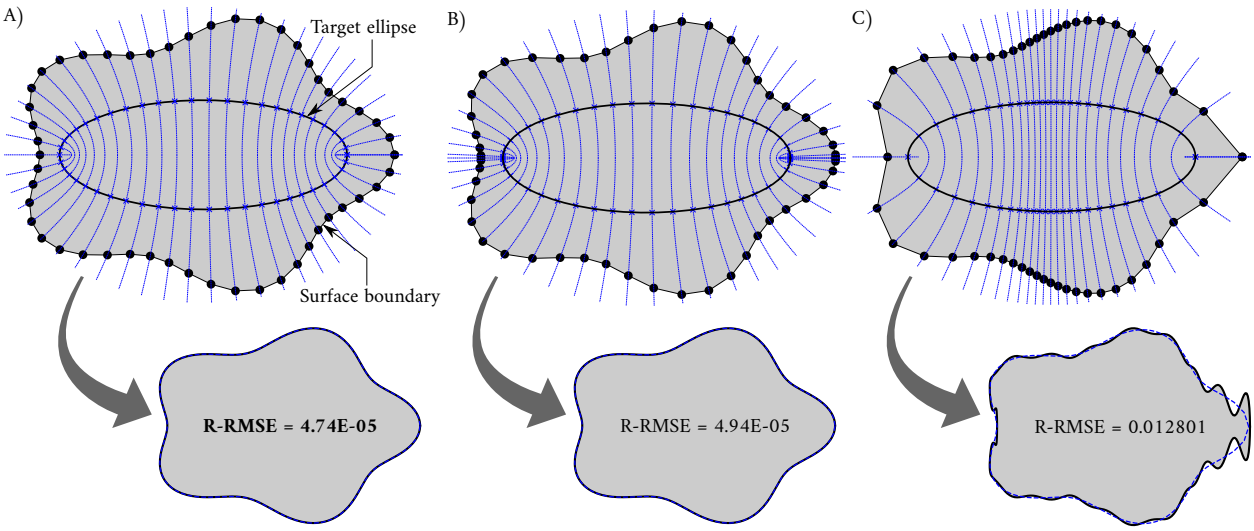


Figure SI-4: Comparing the effect of clustering sampled points in different regions. (A) uniformly sampled target spheroid with equal elliptic-arc length. (B) Densely sampling the target ellipse near high curvature areas (the poles). (C) Densely sampling the target ellipse near low curvature areas. The underneath insets show the reconstruction results using $n_{max} = 20$ and with 161 sampled points for each contour. The herein-shown contours do not reflect the real number of sampled points and are mere visualization contours for the effect of sampling target ellipses.

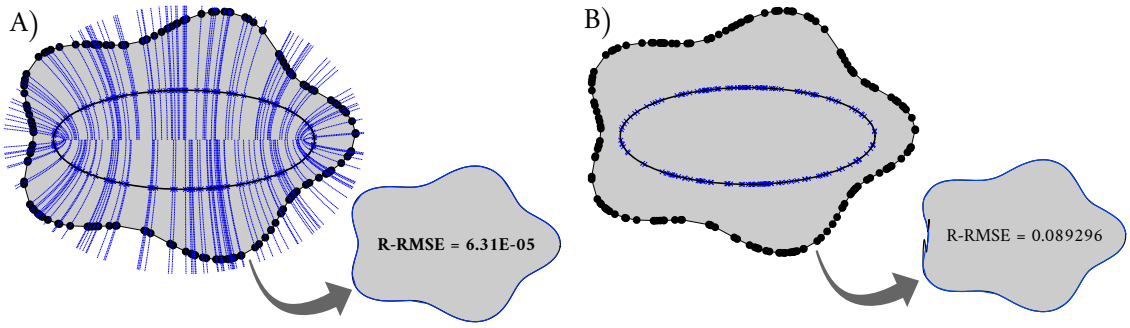


Figure SI-5: Reconstructing contours with radial and hyperbolic mappings of a sampled 161 random points from the 2D contour of the surface with a fixed seed number 5. (A) shows the randomly sampled stone using hyperbolic mapping and the resulting reconstruction. (B) same as (A) but with radial mapping.

# SI-2 Supplemental results

## SI-2.1 Stones reconstruction examples

In this section, we present the rest of the results for the chosen stones from the three datasets. Figure SI-6 is a continuation of Fig. 6 in the main text, where we compare the reconstruction via the traditional SH and the newly proposed SOH-based approaches for Dataset 1. Similarly, Fig. SI-7 is also a continuation of Fig. 8 in the main text, to compare the reconstruction results between the same abovementioned approaches for Dataset 2.

Figure SI-8 is a continuation of Fig. 10 in the main text where we show the results of the reconstruction using c-rSOH approach for the non-star shaped stones in Dataset 3.

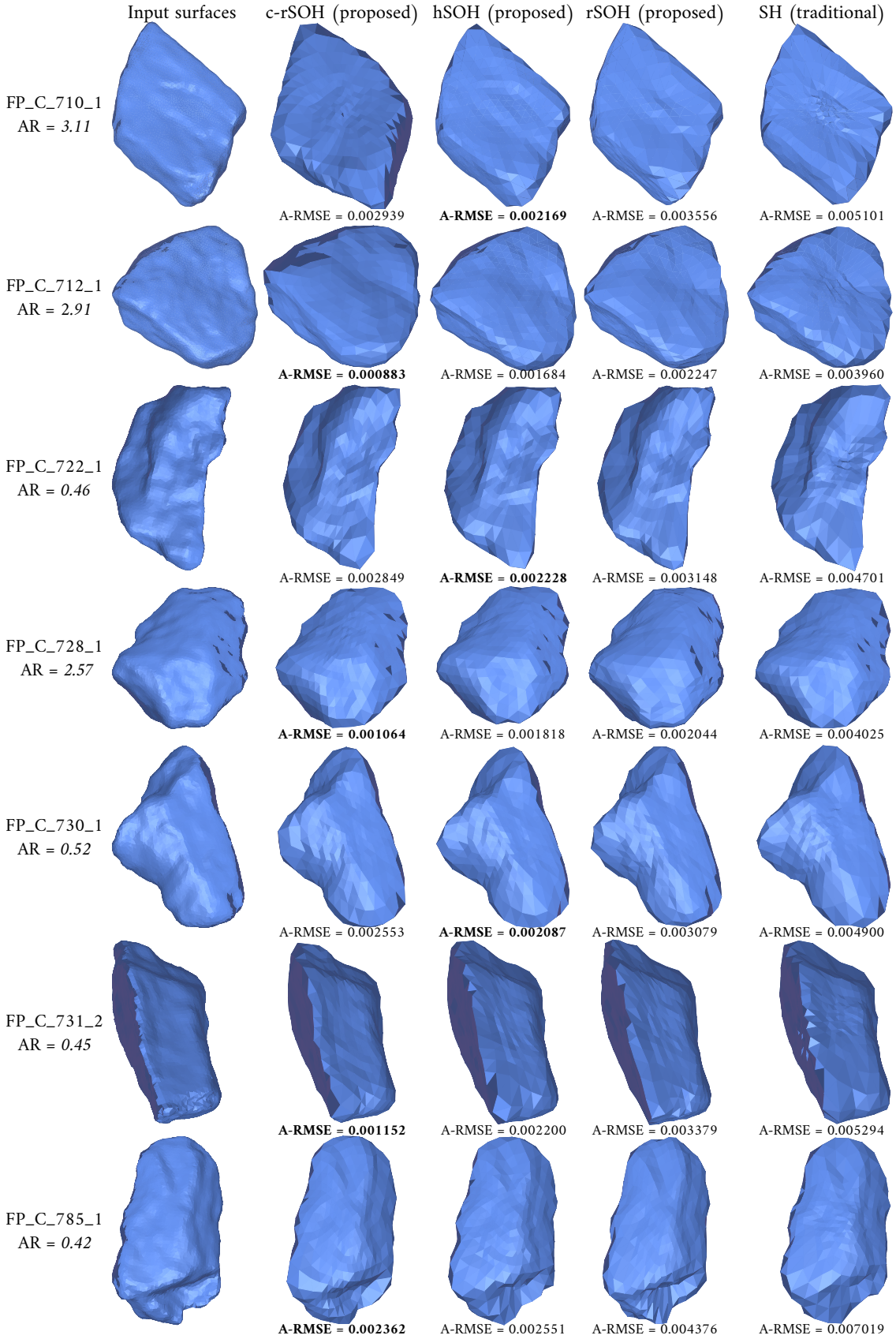


Figure SI-6: Reconstruction of a selected set of SS rubble stones (Saloustros et al., 2023) via the conformal spheroidal approach (c-rSOH, second column), hyperbolic spheroidal approach (hSOH, third column), radial spheroidal approach (rSOH, fourth column), and traditional spherical harmonics (SH, fifth column). The codenames and the fitted aspect ratios (AR) for the stones are shown on the far left annotations. Each reconstructed stone shows the normalized average distances (A-RMSE) below. Boldfaced **A-RMSE** highlights the best reconstruction accuracy.

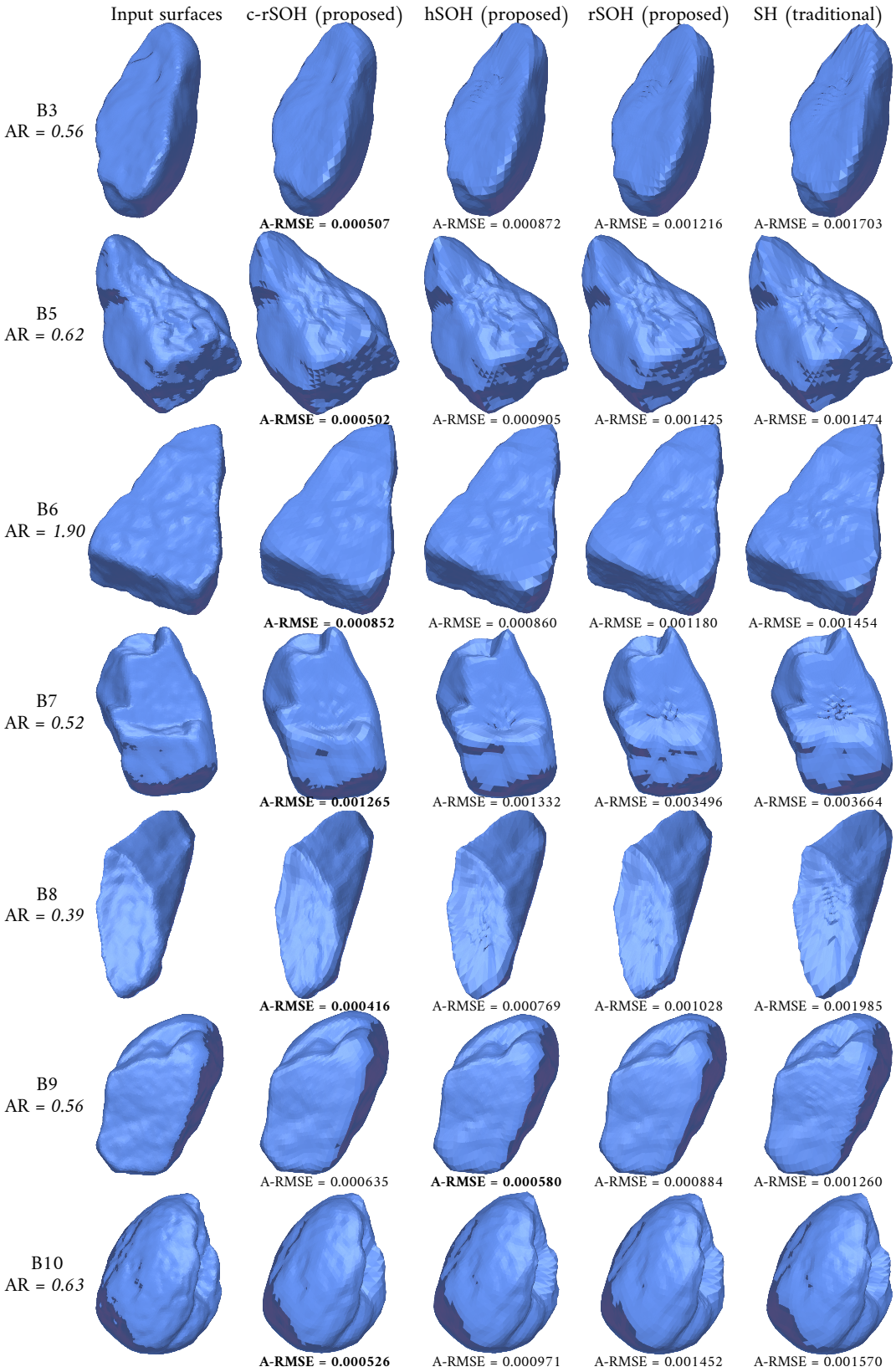


Figure SI-7: Reconstruction of a selected set of SS aggregates (Thilakarathna, 2020) through the conformal- and hyperbolic as well as radial approaches. The first column contains the input surfaces, while the second, third, and fourth are the reconstruction via the spheroidal harmonics c-rSOH, hSOH, and rSOH, respectively, as well as the traditional spherical harmonics (SH) in the fifth column. The left-hand texts show the annotation per stone and the fitted aspect ratio (AR) for the spheroidal coordinates. Each reconstructed stone shows the normalized average distances (A-RMSE) below. Boldfaced **A-RMSE** highlights the best reconstruction accuracy.

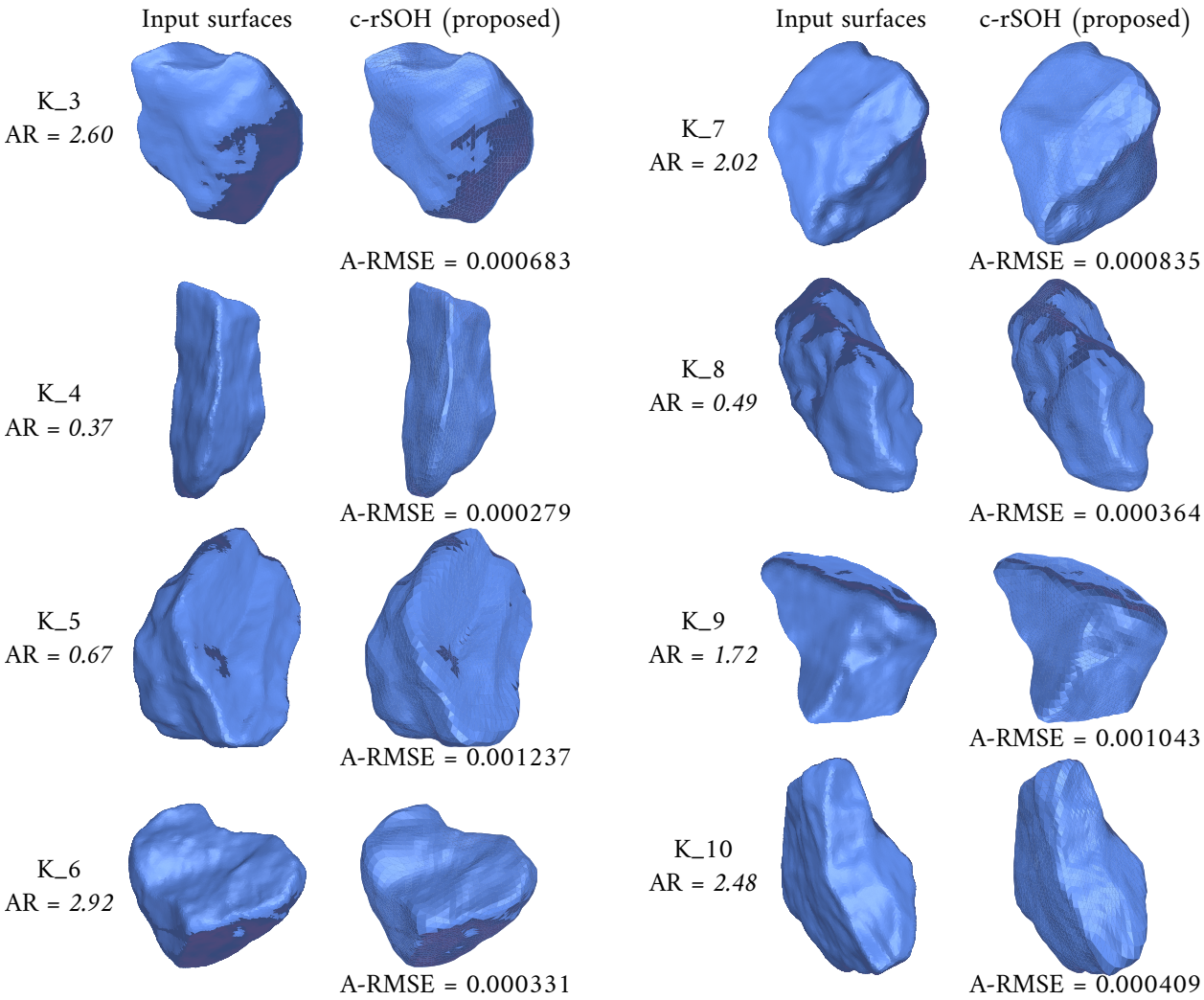


Figure SI-8: Reconstruction of a selected set of rubble stones (Suhr et al., 2020b). using the c-rSOH approach. Each reconstructed stone shows the normalized average distances (A-RMSE) below.

## SI-2.2 Aspect ratio $a/c$ versus RMSE

Figure SI-9 shows the results of the reconstruction accuracy using the rSOH approach for stones of the first dataset (oblate (A) and prolate (B) particles) when varying AR (rSOH is AR-dependent). The estimates of the least-squares strategy in Section 3.2 of the main text give a reasonable solutions for SS particles. From the figure, we notice that the closer the spheroid is to a sphere the larger the reconstruction error. Although not optimal, the spheroidal fitting provides a conveniently fast and good reconstruction making it a valid approach for practical usage for SS particles.

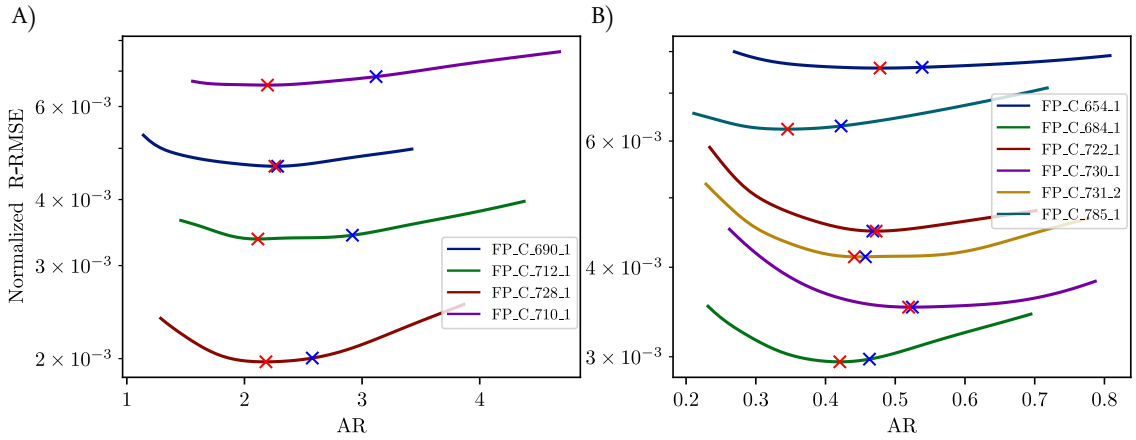


Figure SI-9: Optimization curves for R-RMSE vs. AR for the first dataset retrieved from Saloustros et al. (2023) and reconstructed via the rSOH in Fig. 6 in the main text, and Fig SI-6 above. (A) is the reconstruction for oblate-like particles $a/c > 1$ and (B) for prolate-like ones where $a/c < 1$. Red crosses mark the optimal AR and blue crosses are for the LS fit.

Similar to the presented results of the first dataset, Fig. SI-10 shows an example of the R-RMSE variation with the rSOH approach along with the AR. This figure also explains how insignificant changes in the R-RMSE do reflect some considerable changes in the shape descriptors (see the inset of the same figure) that will undoubtedly affect the estimated fractal dimension of that stone. Figure SI-11 summarizes the results for all the tested stones in the second dataset (Thilakarathna, 2020). The results, however, show some discrepancies between the fit and the optimal AR for the stones B3 and B7. This indeed corresponded to minor osculations as depicted in Fig. SI-7 for the rSOH approach. Nevertheless, the reconstruction quality is still better than the traditional spherical harmonics with radial parameterization.

For the third dataset, the error sensitivity was approached slightly differently from the former two datasets. We studied the effect of the maximum number of smoothing iterations used for the cMCF approach on the final reconstruction RMSE. Figure SI-12(A) shows the stone K_1 (Suhr et al., 2020a) and the stages of mapping the stone (see Section 3.2.4 of the main text). Figure SI-12(B) shows the relation between the cMCF iterations and the reconstruction accuracy of the stone. We can also see that the shape descriptors scatter is less than the former two datasets as the AR itself is not changing much due to iterations as shown in the two insets of the same figure.

As shown in Fig. SI-13(A), most of the stones show better results once we flow the surface with $2-4$ iterations only before applying the radial mapping. As a result, we obtained very good results for more challenging stones like the railway ballast rubbles. Fig. SI-13(B) shows how the AR changes with iterations for both oblates (AR $> 1$) and prolates (AR $< 1$).

## SI-2.3 Conformal parameterization and reconstruction of a visual benchmark

Figure SI-14 depicts the parameterization of the Max Planck bust benchmark surface. For this NSS surface, we used the cMCF approach (Kazhdan et al., 2012). The step size (each time step is an iteration $j$) for the solver was set to $\delta = 0.0005$.

As can be seen in the figure, the surface evolution passes through intermediate stages at each time step (diffeomorphisms) that are equivalent to the input surface (conformal equivalence). The further we flow the

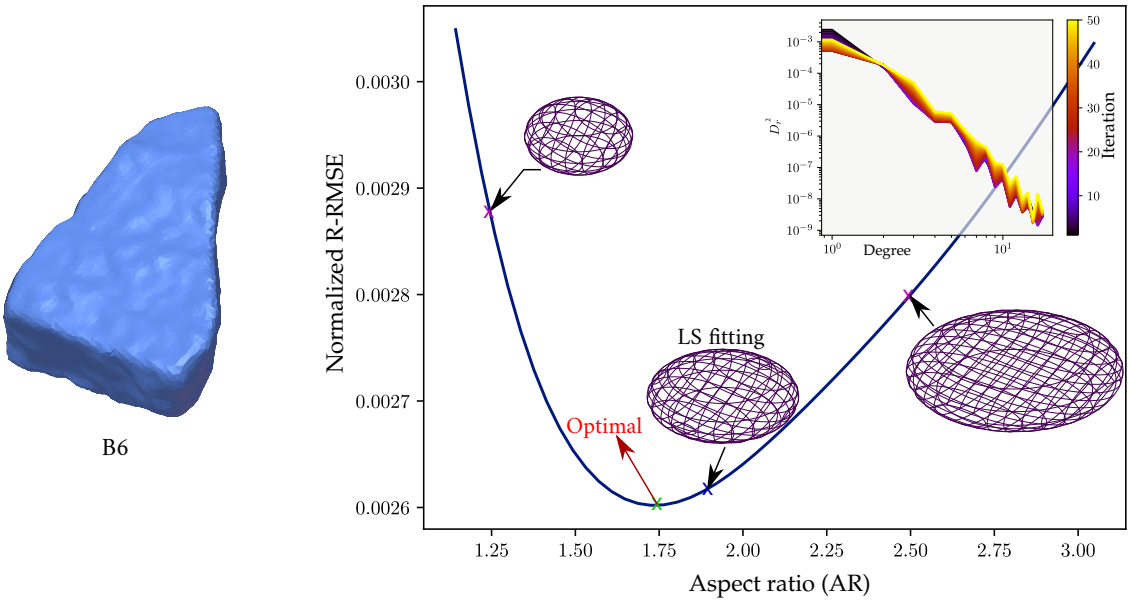


Figure SI-10: The radial normalized R-RMSE vs. the aspect ratio (AR) for stone B6 (Thilakarathna, 2020) reconstructed via rSOH. The inset shows the variation of the shape descriptors as we change the AR from 1.14 $\rightarrow$ 3.04 (the interval was spaned by 50 iterations). The optimal AR was observed to be 1.74, while the one obtained from the least-squares fit was 1.90. As we approach a sphere AR = 1.0 or AR = 3.0 the solution diverges faster. Notice that the optimal error is not 0.0 due to the truncation error ($n_{max} = 20$) and the projection error for finding Fourier weights.

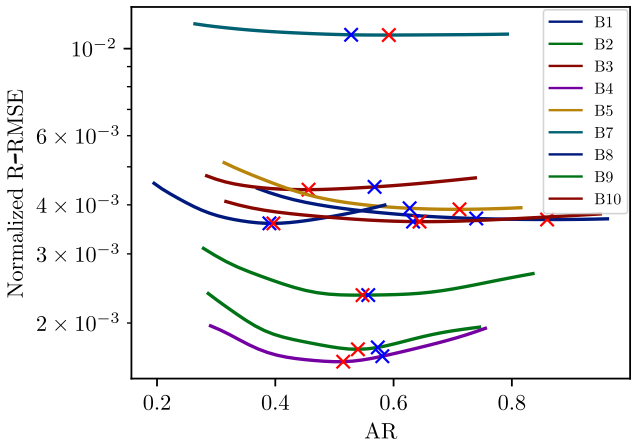


Figure SI-11: rSOH optimization curves for R-RMSE versus AR for the dataset retrieved from Thilakarathna (2020) and reconstructed in Fig. 8 in the main text, and Figure SI-7 above for prolate-like particles where $a/c < 1$. Red crosses mark the optimal AR and blue crosses indicate the aspect-ratio of the least-squares fit.

surface (more iterations) it converges into a sphere, however, with large area distortion. Over time, these almost-spheroidal intermediate shapes become convex and can be used as a point to radially map, see Section 3.2.2 of the main text, the surface into a spheroid without being NSS.

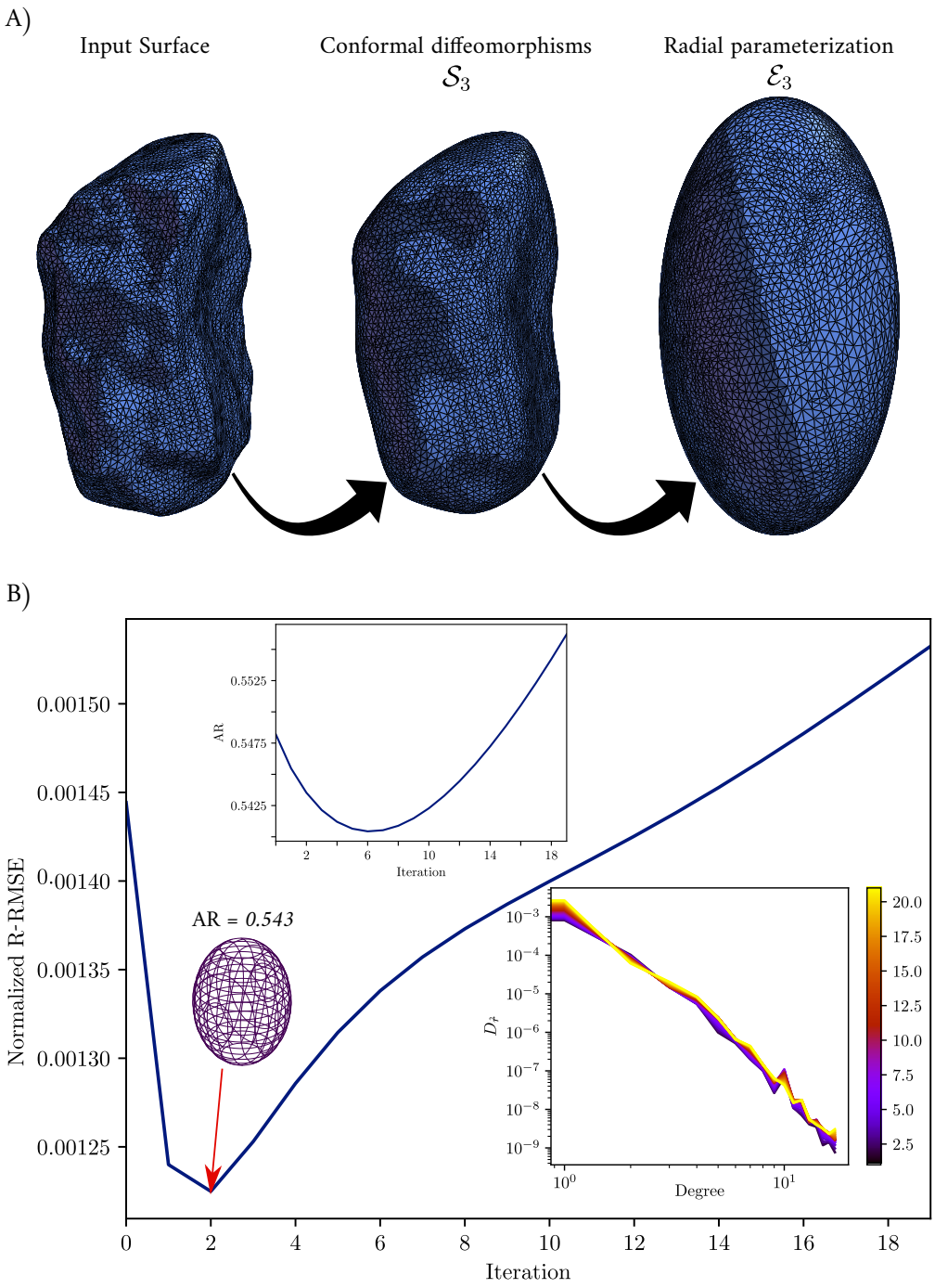


Figure SI-12: (A) depicts the conformal-based parameterization approach for the mesh of stone K_1 (Suhr et al., 2020a); the same stone but different view from Fig. 10 in the main text. (B) Optimization curves for R-RMSE vs. the curvature flow iteration with a time step $\delta = 0.0005$ for the dataset retrieved from Suhr et al. (2020b) and reconstructed in Fig. 10 in the main text, and Fig. SI-8 above. The analysis results of this figure all belong to stone K_1 from the third dataset.

Combining the cMCF approach with the radial projection mapping, see Section 3.2.4 of the main text, becomes handy for mapping NSS objects. Figure SI-15 shows the results of the harmonic decomposition of the herein-proposed visual benchmark. Similar to the SPHARM (Brechbühler et al., 1995) and Shaqfa et al. (2021) the reconstruction at $n = 1$ results in an ellipsoidal shape that can be used for estimating the reconstruction wavelength.

In Fig. SI-15, we have flown the surface using the first ten time steps ($j = 10$), and after that, we applied the proposed radial mapping. We have determined this number of iterations as we obtain an optimal reconstruction at this number of iterations. Again, the process of finding an optimal spheroidal size is not trivial, and it is hard to find without posing the problem as an optimization problem. Finally, we include two videos in the supplemental material that show the cMCF flow and the reconstruction of the same surface.

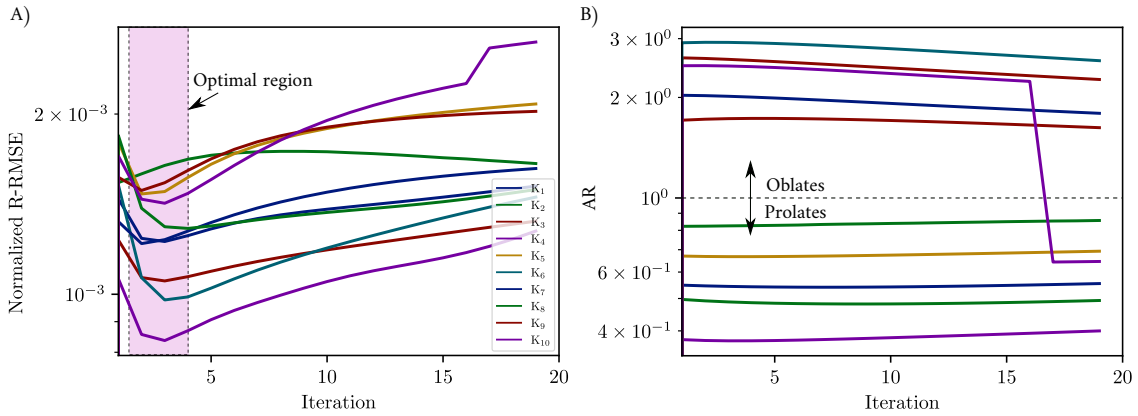


Figure SI-13: Optimization curves for the reconstruction error with respect to the maximum iterations used in the cMCF approach. (A) shows the radial normalized R-RMSE with the cMCF used iterations before applying the radial mapping and analysis process. The used time step here is $\delta = 0.0005$ for the dataset retrieved from Suhr et al. (2020b). (B) shows the change of AR with iterations for oblate and prolate stones. The visual reconstruction results are depicted in Fig. 10 in the main text, and Fig. SI-8 above.

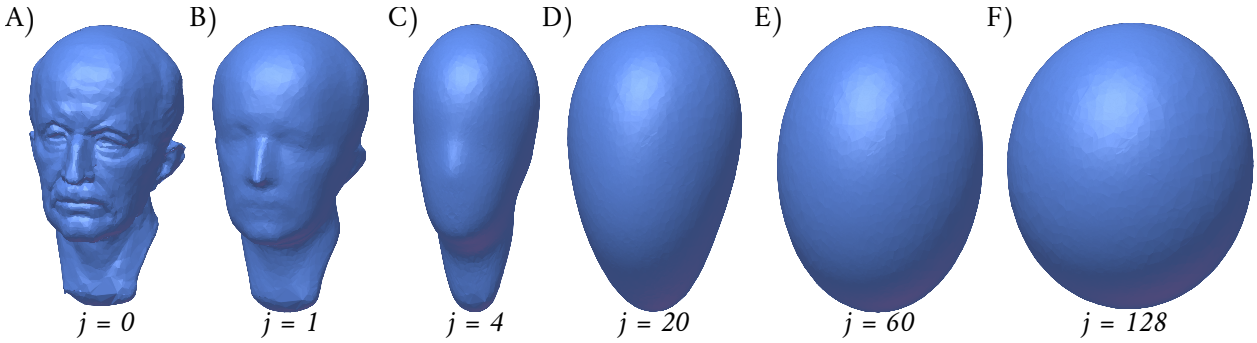


Figure SI-14: The flow of Max Planck bust via the cMCF parameterization (Kazhdan et al., 2012) at different $j$ iterations up to 128 [insets (A) $\rightarrow$ (F)]. As the flow progresses, the surface converges into a sphere $\mathbb{S}^2$. The surfaces of each subset were rescaled to conserve the original surface area of the surface. Notice, at $j = 4$ [inset (C)] the surface became star-shaped and can be radially mapped into a spheroid (i.e., $\mathcal{E}_4$).

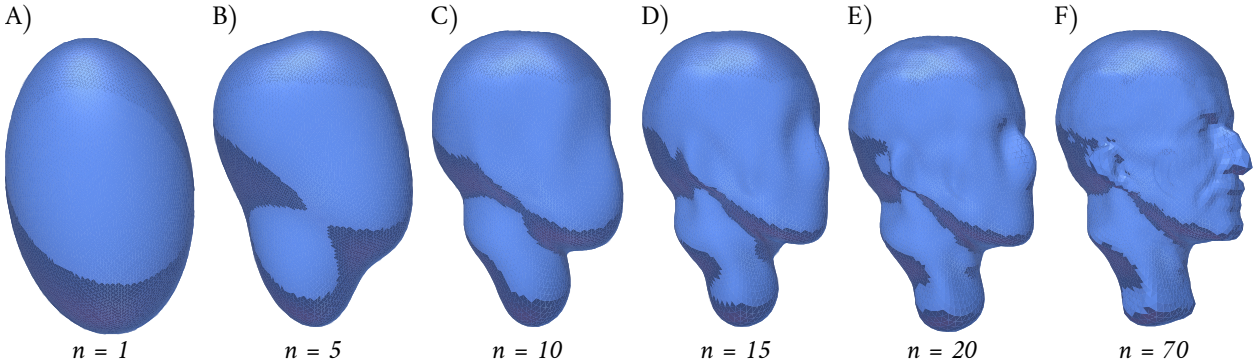


Figure SI-15: Reconstruction of Max Planck bust as a visual benchmark via the spheroidal harmonics. For the mapping, we used the cMCF whence $j = 10$ and $\delta = 0.0005$. With these settings, we were able to be convergent up to $n_{max} = 70$ degrees.

# References


Brechbühler, C., Gerig, G., Kübler, O.. Parametrization of closed surfaces for 3-D shape description. Computer Vision and Image Understanding 1995;61(2):154–170.

Kazhdan, M., Solomon, J., Ben-Chen, M.. Can mean-curvature flow be made non-singular? Eurographics Symposium on Geometry Processing 2012 2012;URL: https://arxiv.org/abs/1203.6819. doi:10.48550/ARXIV.1203.6819.

Kuhl, F.P., Giardina, C.R.. Elliptic fourier features of a closed contour. Computer Graphics and Image Processing 1982;18(3):236–258. URL: http://dx.doi.org/10.1016/0146-664X(82)90034-X. doi:10.1016/0146-664x(82)90034-x.

Mollon, G., Zhao, J.. Fourier–voronoi-based generation of realistic samples for discrete modelling of granular materials. Granular Matter 2012;14(5):621–638. URL: http://dx.doi.org/10.1007/s10035-012-0356-x. doi:10.1007/s10035-012-0356-x.

Saloustros, S., Settimi, A., Cabriada Ascencio, A., Gamerro, J., Weinand, Y., Beyer, K.. Dataset for geometrical digital twins of the as-built microstructure of three-leaf stone masonry walls with laser scanning. 2023. URL: https://zenodo.org/record/7093710. doi:10.5281/ZENODO.7093710.

Shaqfa, M., Choi, G.P.T., Beyer, K.. Spherical cap harmonic analysis (SCHA) for characterising the morphology of rough surface patches. Powder Technology 2021;393:837–856. URL: https://www.sciencedirect.com/science/article/pii/S0032591021006720. doi:https://doi.org/10.1016/j.powtec.2021.07.081.

Suhr, B., Six, K., Skipper, W.A., Lewis, R.. 3d scans of two types of railway ballast including shape analysis information. 2020a. URL: https://zenodo.org/record/3689592. doi:10.5281/ZENODO.3689592.

Suhr, B., Skipper, W.A., Lewis, R., Six, K.. Shape analysis of railway ballast stones: curvature-based calculation of particle angularity. Scientific Reports 2020b;10(1). URL: https://doi.org/10.1038/s41598-020-62827-w. doi:10.1038/s41598-020-62827-w.

Thilakarathna, S.. 3d scanned aggregates. 2020. URL: https://data.mendeley.com/datasets/x5dbx8yxdw/1. doi:10.17632/X5DBX8YXDW.1.